



ORIGINAL ARTICLE

Damping Properties of Selective Laser-Melted Medium Manganese Mn–xCu Alloy

Jingjing Yang,¹ Tongbo Wei,¹ Chunyang Zhao,² Hailong Liang,² Zemin Wang,² and Chenyu Su¹

Abstract

In this work, selective laser melting (SLM) technology was applied to directly realize the *in situ* synthesis of medium manganese Mn–xCu ($x = 30\text{--}40$ wt.%) alloys based on the blended elemental powders. The effects of heat treatment on the microstructural evolution and damping properties of the SLMed Mn–xCu alloys were investigated. The metastable miscibility gap was studied by thermodynamic modeling and microhardness measurement. The results showed that γ -(Mn, Cu) phase with dendritic arm spacing (DAS) of $0.9\text{--}1.2\ \mu\text{m}$ was the main constituent phase in the as-SLMed alloys, which was one to two orders of magnitude finer than those of the as-cast samples. Aging at $400\text{--}480^\circ\text{C}$ for the Mn–30%Cu or 430°C for Mn–40%Cu alloys can induce spinodal decomposition, martensitic transformation, and α -phase precipitation, whose direct evidence was provided for the first time by transmission electron microscopy and 3D atom probe tomography in the work. The miscibility gap obtained from thermodynamics calculation was basically consistent with the microhardness results for the SLMed Mn–xCu alloys. Solution and aging (SA) treatment can improve the microstructure, tensile and damping properties of the SLMed Mn–xCu alloys more obviously than aging treatment. A 2.3–2.8 and 4.3–4.5 times increase was produced in damping capacity in the aged SLMed and SLMed+SAed Mn–xCu samples, respectively.

Keywords: selective laser melting, damping property, Mn–Cu alloys, heat treatment, metastable miscibility gap

Introduction

MN–CU ALLOYS HAVE BEEN attracting significant attention in various fields of application, such as radiofrequency communications, sensors and actuators, energy harvesters, and biomedical devices due to their excellent mechanical properties and high damping capacity.^{1–3} Their excellent damping capacity mainly originates from the high mobility of {101} twin boundaries induced by martensitic phase transformation with low critical twinning/detwinning stress^{4,5} and large tetragonal distortion ($1 - c/a$).^{6,7} Therefore, martensitic phase transformation is the basis of the damping capacities in the Mn–Cu-based alloys.

However, the martensitic transformation start temperature (M_s) is linearly dependent on Mn content in the Mn–Cu-based alloys.^{8,9} The M_s can be above room temperature only when the Mn content (x_{Mn}) in the alloys is >82 at. %.^{10–12} However, a high Mn content (>80 at. %) also leads to the deterioration of ductility, corrosion resistance, mechanical

behaviors, and machining ability.¹³ Consequently, the Mn content is usually restricted to $50\text{--}70$ at.% in the developed commercial Mn–Cu-based alloys, such as Sonoston, Incramute, and M2052,^{14–16} which were referred to as medium manganese Mn–Cu alloys. Fortunately, Mn content can also be improved by spinodal decomposition to form nanoscale Mn-enrichment and Cu-enrichment regions in the alloys^{17,18} upon aging (usually $400\text{--}600^\circ\text{C}$ ¹⁹). Such demixing of Mn-enrichment and Cu-enrichment regions was derived from the metastable miscibility gap in the Mn–Cu binary phase diagram.^{20,21}

However, the α -Mn phase is also precipitated during aging resulting in a decrease in Mn content in Mn-enrichment regions, which affects the formation of martensitic transformation twins, hinders the movement of the twin interface, and thus weakens the damping property of the alloy. Therefore, heat treatment becomes necessary to increase the Mn content in the Mn-rich regions, avoid the emergence of the α -Mn phase, and ultimately control the damping property of

¹The Institute of Technological Sciences, Wuhan University, Wuhan, China.

²Wuhan National Laboratory for Optoelectronics, Huazhong University of Science and Technology, Wuhan, China.

the medium manganese Mn–Cu-based alloys. Especially, the metastable miscibility gap of the alloys should be determined accurately to help figure out the appropriate heat treatment parameters.

Traditionally, Mn–Cu-based alloys are prepared by casting or vacuum induction melting (VIM), then hot forging or rolling, followed by solid solution treatment to obtain a homogeneous microstructure consisting of equiaxed γ -(Mn, Cu) grains. Finally, aging treatment is applied to induce spinodal decomposition and resulting martensitic transformation to produce martensitic twin structures.²² Recently, the emerging laser additive manufacturing technology has been proved a feasible way to prepare the metals and alloys.^{23–25} As one of the typical laser additive manufacturing techniques, selective laser melting (SLM) has been widely reported as a means of producing net-shape complex structures with the advantages, including easy melting of refractory metals, finishing unlimited geometrically complex parts in one step, and realizing the design and adjustment of the alloy composition.^{26–28} Also, the damping capacity of the Mn–Cu-based alloys with dendrite structure is higher compared with equiaxed grains due to compositional segregation upon appropriate aging treatment.²⁹

It is easy to obtain the dendrites and finely nonequilibrium phases under rapid solidification conditions with a cooling rate of 10^{3-8} K/s during SLM.^{30,31} Therefore, SLM may be one of the most potential new technologies for preparing high-density Mn–Cu alloys with excellent comprehensive performances. However, the microstructures of the SLMed Mn–Cu-based alloys would be different from those produced by traditional thermomechanical processes because of these characteristics of SLM process, including high temperature gradient (10^6 K/m), rapid solidification cooling rates, and

complex heat history.³² Hence, the suitable heat treatment parameters for the SLMed Mn–Cu-based alloys may also be different from those for the conventional thermomechanical-processed ones.

In this work, SLM is first applied to realize the *in situ* synthesis of Mn directly $-x$ Cu ($x = 30\text{--}40$ wt.%), alloys based on Mn and Cu mixed elemental powders. Then, the microstructural evolution and phase composition of the SLMed Mn– x Cu samples under various heat treatments were investigated to determine the metastable miscibility gaps of the alloys. Finally, the microhardness, tensile, and damping properties of the SLMed samples were analyzed to explore the suitable heat treatment parameters to control and improve the comprehensive performances.

Experimental

Materials and equipment

The original materials were commercially available high-purity irregularly shaped manganese powders (99.89 wt.% Mn) and spherical copper powders (99.72 wt.% Cu) produced by the atomization method shown in Figure 1a and b. The Mn and Cu powders were mixed in various formulas in a small planetary ball mill for 2.5 h with a rotating speed of 300 r/min at ambient temperature and pressure in atmospheric air. The ball-to-powder ratio of 2:1 was used with alumina ($3.5\text{--}3.9$ g/cm³) and Zirconia (5.8 g/cm³) balls as grinding media under three different ball diameters of 3, 5, and 8 mm in diameter.

The SLM experiments were conducted on a self-developed machine (LSNF-2), consisting mainly of a continuous wave IPG YLR-500 fiber laser, an automatic powder delivery system, a building platform, and a computer system for process control.^{33,34} The deposition processes were conducted to

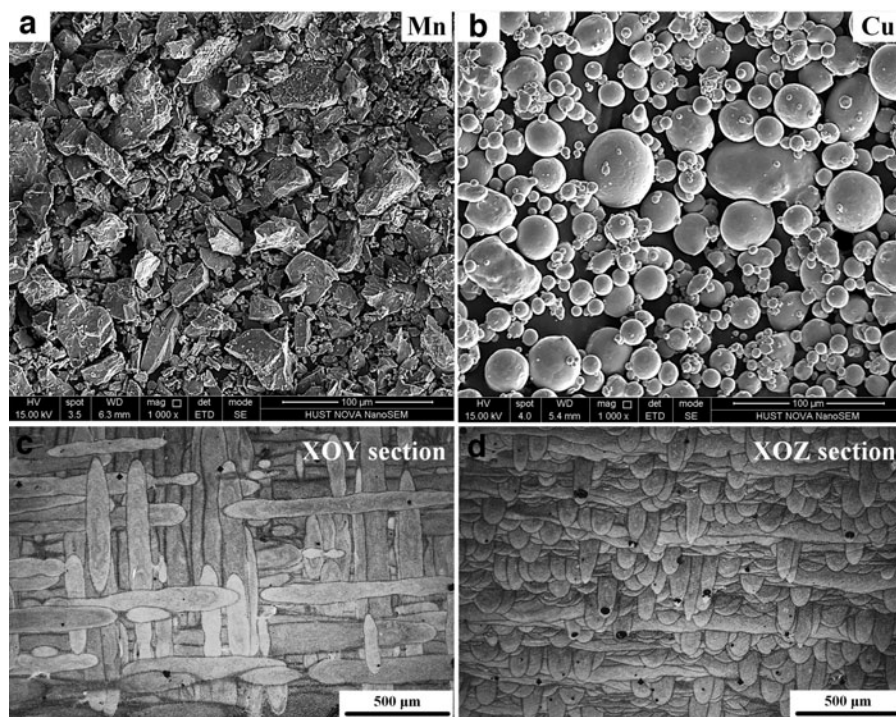


FIG. 1. The morphologies of the original Mn (a) and Cu (b) powders, scanning tracks (c) and molten pools (d) of the as-SLMed Mn– x Cu alloy. SLM, selective laser melting.

TABLE 1. THE HEAT TREATMENT PARAMETERS USED IN THE WORK

Group	T_S , °C	t_S , h	Cooling type	T_A , °C	t_A , h	Cooling type
Age	—	—	—	370–530 430	2 0.5–11	Air cooling
SA	900	1	Water quenching	370–530 430	2 0.5–11	

SA, solution and aging.

manufacture a series of Mn-xCu samples ($x=30$ and 40 wt.%) on a Cu substrate in an argon environment with oxygen content controlled well below 100 ppm. Almost full-dense Mn-xCu samples subjected to SLM only (hereafter as-SLMed) can be fabricated under the proper processing parameters. Then, the SLMed Mn-xCu samples were heat treated in a KSL-1400X-A2 muffle furnace at a heating rate of 10°C/min with the following two groups of schedules, that is, aging or solution and aging (hereafter SA) treatments. T_S , T_A , t_S , and t_A represent the temperature and time of SA treatments in Table 1, respectively.

One group of samples were only aged at a temperature ranging from 370°C to 530°C for 2 h with air cooling (hereafter aged SLMed samples). The other group was first subjected to solution treatment at 900°C for 1 h and then quenched into the water, followed by aging treatment at 370–530°C for 2 h or at 430°C for 1–10 h under air cooling (hereafter SLMed+SAed samples).

Microstructure characterization and performance evaluation

The microstructural characterization of the as-SLMed, aged SLMed, and SLMed+SAed Mn-xCu samples was

conducted by a Motic 2000 MET optical microscope, a Zeiss G300 scanning electron microscope (SEM) equipped with energy-dispersive spectroscopy (EDS), and a Tescan Mira3 SEM. Phase identification of all the samples was performed by X'Pert PRO X-ray diffraction (XRD) using a Cu K α radiation with a step size of 0.02° and a dwell time of 1 s per step. The microstructure of the SLMed+SAed Mn-30%Cu sample was also observed by an FEI Tecnai G2 F30 Transmission Electron Microscope (TEM) at 300 kV. The chemical composition of the SLMed+SAed Mn-30%Cu sample was investigated at a sub-nanometer scale by 3D atom probe tomography (APT) analysis using a LEAPTM 3000X HR (Oxford nanoScience Ltd, Milton Keynes, United Kingdom).

The needle-shaped specimen for APT was prepared by using an FEI Helios NanoLab 600i DualBeam focused-ion-beam instrument. The APT acquisition was performed in voltage mode at 60 K with a pulse fraction of 20%, a pulse repetition rate of 2 kHz, and a target detection rate of 0.4%. The reconstruction of 3D atom maps, visualization, and all data analyses were performed using the IVAS^R 3.6.14 software package.

Microhardness measurements were conducted using an HVS-1000Z microhardness tester with a loading range between 10 gf and 1 Kgf. The microhardness was calculated as

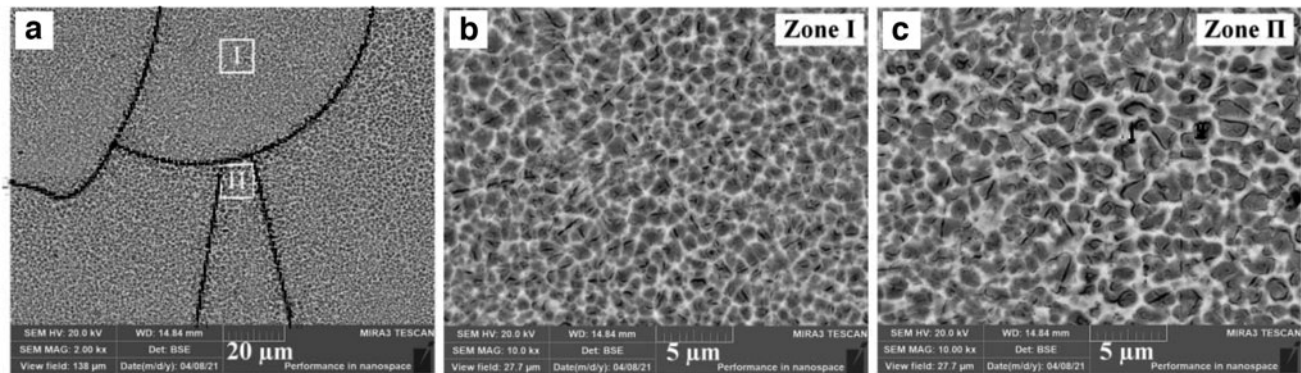


FIG. 2. The BSE images of the as-SLMed Mn-30%Cu alloy; the molten pool boundaries were indicated by yellow dotted lines in (a); (b, c) are the magnifications of the areas marked by I and II in (a), respectively; the table is the chemical components of the points indicated in (c) detected by EDS. EDS, energy-dispersive spectroscopy. BSE, back-scattered electron.

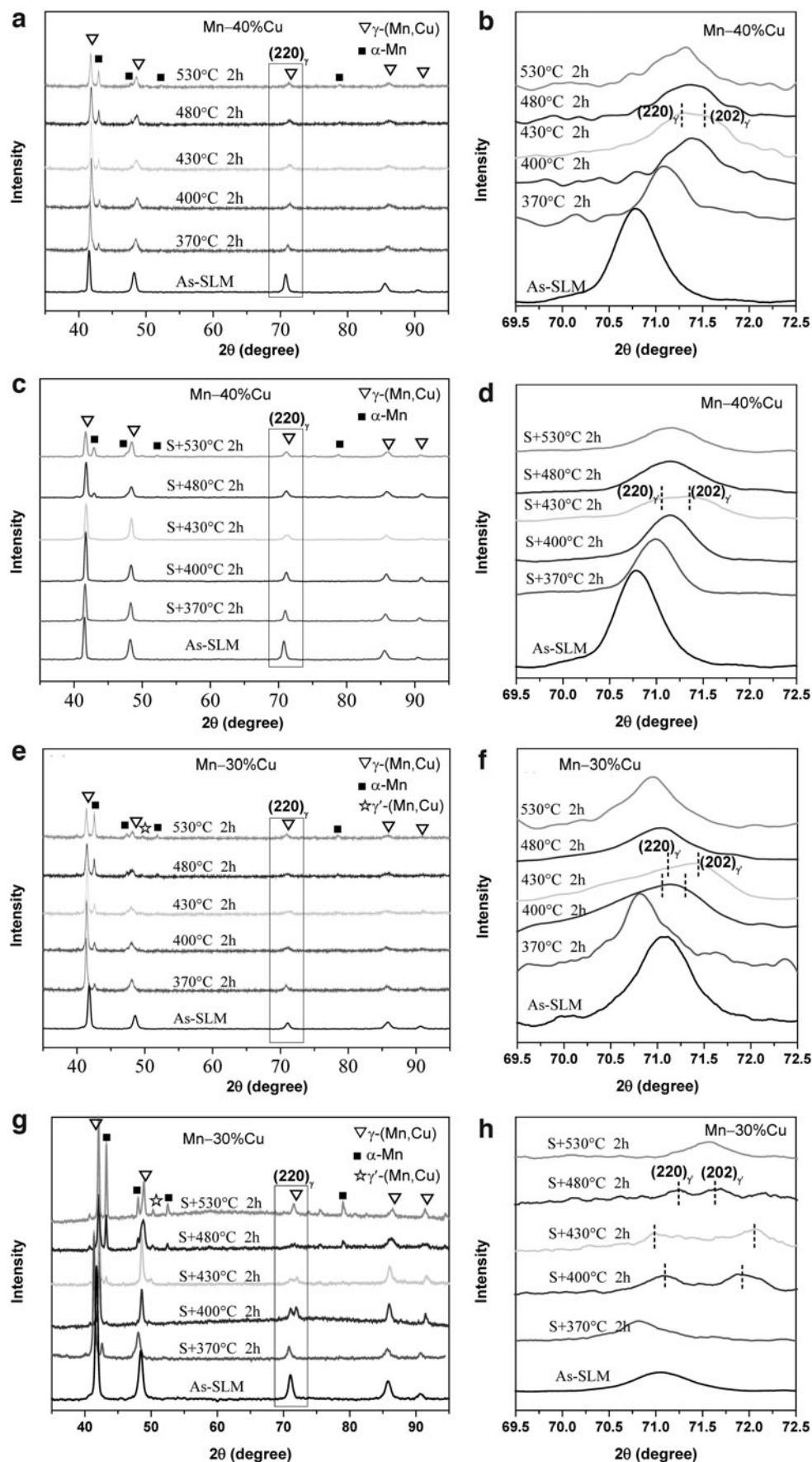


FIG. 3. XRD patterns of as-SLMed, aged SLMed (a, b, e, f), and SLMed+SAed (c, d, g, h) Mn-40%Cu (a-d) and Mn-30%Cu (e-h) alloys under various aging temperatures; (b, d, f, h) are local magnifications of characteristic diffraction peaks of (a, c, e, g), respectively; S represents solution treatment. SA, solution and aging; XRD, X-ray diffraction.

TABLE 2. THE PHASE COMPOSITIONS OF THE AS-SLM_{ED}, AGED SLM_{ED}, AND SLM_{ED}+SA_{ED} MN-*x*CU ALLOYS

State	Mn-40%Cu		Mn-30%Cu	
	T _A (°C)	Phase	T _A (°C)	Phase
Aged SLM _{ED}	370, 400, 480, 530	γ + α	370, 480, 530	γ + α
SLM _{ED} +SA _{ED}	430	γ + α + γ'	400-430	γ + α + γ'
	370-400	γ	370	γ + α
	430	γ + γ'	400-480	γ + α + γ'
As-SLM	480-530	γ + α	530	γ + α
	—	γ	—	γ

SLM, selective laser melting.

the maximum load divided by the projected area of the indentation. For each load step, ten indentations were done, and their average value was used to represent the hardness. The damping property (internal friction, $\tan \delta$) of all the samples with a size of $30 \times 3 \times 1 \text{ mm}^3$ was measured on a TA-Q800 Dynamic Mechanical Analyzer in the single cantilever mode with a constant frequency (f) of 1 Hz and strain amplitude ranging from 0 to 900×10^{-6} at ambient temperature.

Modeling and calculating of the phase diagram

Thermochemical modeling studies were done by using FactSage™ 8.0 software. The binary phase diagram of the Mn-Cu system was calculated through the Phase Diagram calculation module of the software using FSstel database. The Equilib module of the software was used in adiabatic conditions ($\Delta H = 0$, 1 atm), and the temperature was set from 200°C to 1400°C.

Also, the thermodynamic evaluation of the Mn-Cu system was performed in the present work. Based on a substitutional model, the dependence of the molar Gibbs free energy for the φ phase (G^φ) on temperature (T) and concentration (x_{Mn}) was described by Shi *et al.*⁶:

$$G^\varphi = x_{\text{Mn}}G_{\text{Mn}}^0 + (1 - x_{\text{Mn}})G_{\text{Cu}}^0 + RT(x_{\text{Mn}}\ln x_{\text{Mn}} + (1 - x_{\text{Mn}})\ln(1 - x_{\text{Mn}})) + \Delta G_{\text{exc}}^\varphi(x_{\text{Mn}}, T) \quad (1)$$

where G_{Mn}^0 and G_{Cu}^0 are Gibbs energies of pure Mn and Cu, which can be taken from the Scientific Group Thermodata Europe database³⁵; $\Delta G_{\text{exc}}^\varphi(x_{\text{Mn}}, T)$ is the excess Gibbs free energy, which can be calculated using a Redlich-Kister polynomial³⁶

$$\Delta G_{\text{exc}}^\varphi(x_{\text{Mn}}, T) = (1 - x_{\text{Mn}})x_{\text{Mn}} \sum_{i=0}^n (1 - 2x_{\text{Mn}})^i (A_i + B_i T + C_i T \ln(T)) \quad (2)$$

where i is the power of the Redlich-Kister polynomial; A_i , B_i , and C_i are coefficients of the model. The optimized parameters for the phase γ -(Mn, Cu) of the Mn-Cu system can be taken from reference.³⁶ Hence, the miscibility gap can be obtained by taking the second partial derivative of the molar Gibbs free energy (G^φ) with respect to the variable x_{Mn} .

Results and Discussion

The microstructure of the as-SLM_{ED} alloy

The as-SLM_{ED} Mn-*x*Cu cuboid samples without cracks can be manufactured under a relatively wide processing window. Micropores (9–50 μm in size) were observed in the as-SLM_{ED} samples in Figure 1c and d, showing good processability of laser additive manufacturing for the Mn-*x*Cu alloys based on the blended elemental powders. The mutually vertical scanning tracks were observed on the XOY section due to the applied hatch spacing of 90° in Figure 1c. The regular molten pool boundaries were seen on the XOZ section in Figure 1d.

In Fig. 2a, the microstructure of the as-SLM_{ED} Mn-*x*Cu alloys are mainly composed of γ -(Mn, Cu) cellular dendrite structure. The DAS was measured to be ~ 0.9 and $\sim 1.2 \mu\text{m}$ in the interior (Fig. 2b) and at the boundary (Fig. 2c) of the molten pool, respectively, due to the differences in

TABLE 3. THE LATTICE PARAMETERS OF THE F.C.T.- γ' PHASE (A AND C) AND F.C.C.- γ PHASE (A_0)

Composition	State	T _A	f.c.t.- γ'		f.c.c.- γ	
			a (Å)	c (Å)	$l - c/a$	a_0 (Å)
Mn-40%Cu	Aged SLM _{ED}	430°C	3.7422	3.7198	0.0060	3.7401
	SLM _{ED} +SA _{ED}	430°C	3.7523	3.7251	0.0072	3.7457
Mn-30%Cu	Aged SLM _{ED}	400°C	3.7523	3.7298	0.0060	3.7771
	SLM _{ED} +SA _{ED}	430°C	3.7499	3.7204	0.0079	3.7703
		400°C	3.7508	3.6759	0.0200	3.7119
		430°C	3.7555	3.6612	0.0251	3.7108
		480°C	3.7435	3.7093	0.0091	3.7174

f.c.c., face center cubic; f.c.t., face centered tetragonal.

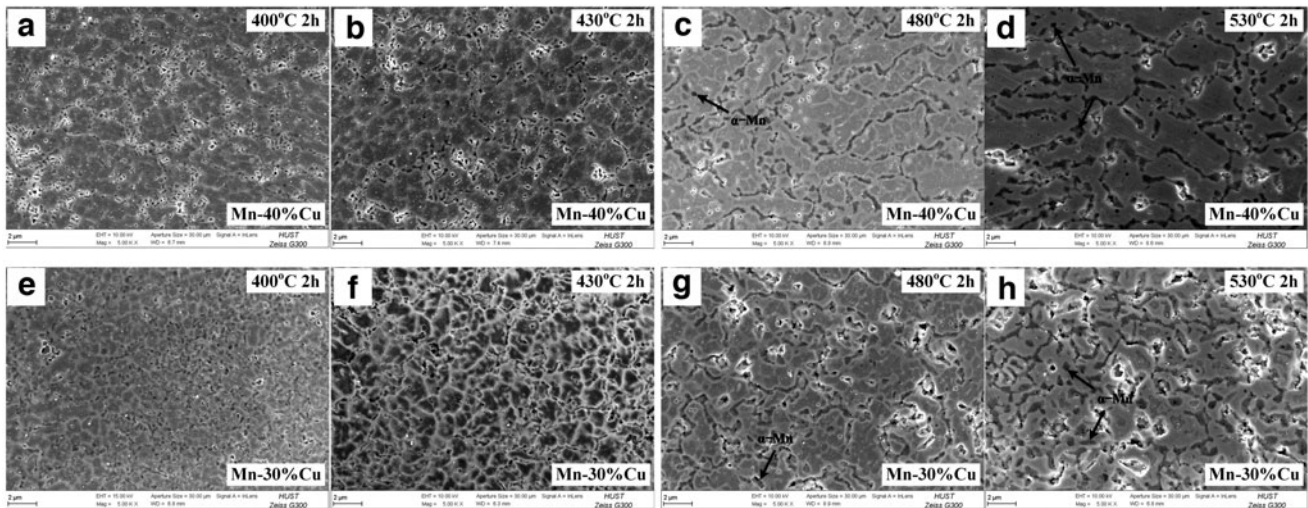


FIG. 4. The microstructures of the aged SLMed Mn-40%Cu (**a-d**) and Mn-30%Cu (**e-h**) alloys at $T_A=400-530^{\circ}\text{C}$.

temperature gradient and solidification velocity between them. Besides, the compositional segregation between the dendritic and interdendritic zones was observed in the obtained back-scattered electron images. Based on the chemical composition analysis by EDS, the dendritic (point 2 in Fig. 2c) and interdendritic (point 1 in Fig. 2c) zones possessed relatively higher and lower Mn contents, respectively. As the melting point of Mn ($1244^{\circ}\text{C} \pm 3^{\circ}\text{C}$) is higher compared with Cu ($1083.4^{\circ}\text{C} \pm 0.2^{\circ}\text{C}$), Mn-rich γ -(Mn, Cu) first precipitated to form the dendritic phase during the rapid solidification process of SLM. Then, Cu-rich γ -(Mn, Cu) phase precipitated along with the interdendritic areas. Then, the formed Mn-rich and Cu-rich γ -(Mn, Cu) phases were retained to ambient temperature under the nonequilibrium solidification condition of SLM.

Figure 3 exhibited XRD patterns of the as-SLMed, aged SLMed, and SLMed+SAed Mn- x Cu samples. The face center cubic (*f.c.c.*) structure of the γ -(Mn, Cu) phase is the main constituent phase in all the samples. Only the γ -(Mn, Cu) phase was detected in the as-SLMed Mn- x Cu alloys. The

peaks of the α -Mn were also observed in the XRD patterns of the aged SLMed alloys (Fig. 3a, b, e, f). Based on the relative peak intensity between the γ -(Mn, Cu) and the α -Mn phases, the volume fractions of the α -Mn phase increased with increasing T_A from 370°C to 530°C in the aged SLMed alloys. Moreover, the fraction of the α -Mn phase was always higher in the Mn–30%Cu samples than those in the Mn–40%Cu samples under the same heat treatment states. The local magnifications in 69.5–72.5° are shown in Figure 3b, d, f, and h. The (220) characteristic diffraction peak of the γ -(Mn, Cu) phase broadened as $T_A=430^\circ\text{C}$ for the aged SLMed Mn–40%Cu (Fig. 3b) or $T_A=400\text{--}430^\circ\text{C}$ for the Mn–30%Cu samples (Fig. 3f). The broadening of (220) diffraction peak was closely associated with the martensitic transformation of $(220)_{\gamma\text{-(Mn, Cu)}} \rightarrow (220)_{\gamma'\text{-(Mn, Cu)}} + (202)_{\gamma'\text{-(Mn, Cu)}}$.

In Fig. 3c and g, the obvious peaks of the α -Mn phase was not detected until at 480°C for SLMed+SAed Mn–30%Cu or 530°C for Mn–40%Cu alloys. As compared with the aging treatment, SA treatment reduced the contents of the α -Mn phase in the samples significantly. Similarly, the (220)

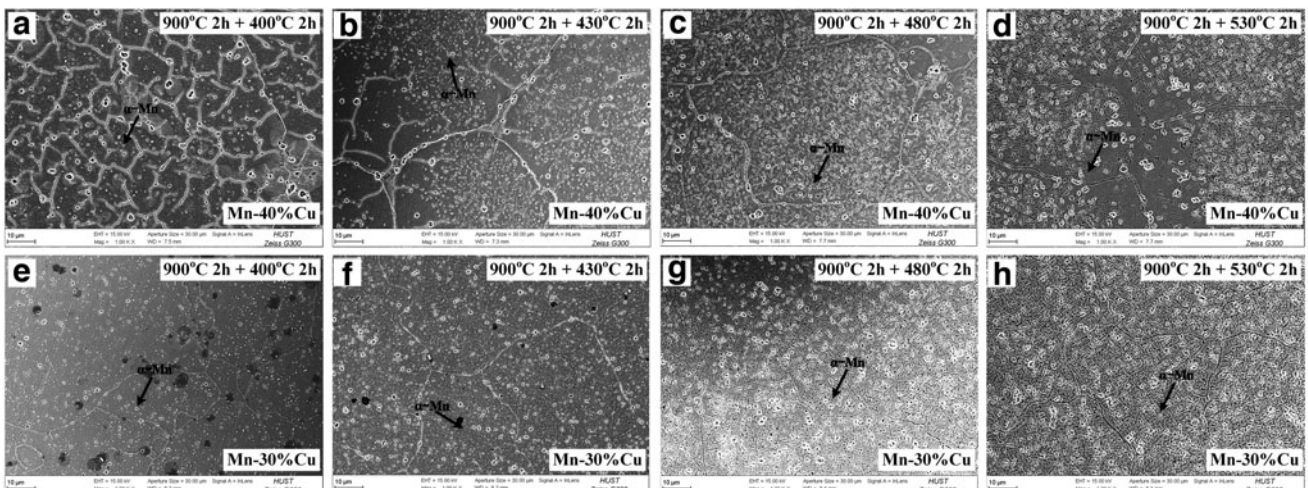


FIG. 5. The microstructures of the SLMed+SAed Mn-40%Cu (**a-d**) and Mn-30%Cu (**e-h**) alloys at $T_A = 400-530^\circ\text{C}$.

TABLE 4. THE AVERAGE GRAIN SIZE OF THE SLM_{ED}+SA_{ED} Mn–xCu ALLOYS AT VARIOUS AGING TEMPERATURES

SA	900°C×1 h + 400°C×2 h	900°C×1 h + 430°C×2 h	900°C×1 h + 480°C×2 h	900°C×1 h + 530°C×2 h
Mn–40%Cu	89.4 μm	87.9 μm	99.1 μm	113.4 μm
Mn–30%Cu	72.4 μm	99.2 μm	102.0 μm	103.3 μm

diffraction peak of the γ -(Mn, Cu) phase also broadened only at $T_A = 430^\circ\text{C}$ in the SLM_{ED}+SA_{ED} Mn–40%Cu alloys (Fig. 3d). Moreover, the splitting of (220) diffraction peak of γ -(Mn, Cu) phase, that is, $(220)_{\gamma-(\text{Mn}, \text{Cu})} \rightarrow (220)_{\gamma'-(\text{Mn}, \text{Cu})} + (202)_{\gamma'-(\text{Mn}, \text{Cu})}$, was detected at $T_A = 400\text{--}480^\circ\text{C}$ in the SLM_{ED}+SA_{ED} Mn–30%Cu alloys (Fig. 3h). Table 2 summarizes the phase composition of the as-SLM_{ED}, aged SLM_{ED}, and SLM_{ED}+SA_{ED} Mn–xCu alloys based on the XRD results in Figure 3. It can be concluded that the spinodal decomposition of γ -(Mn, Cu) \rightarrow Mn-enrichment γ -(Mn, Cu) + Cu-enrichment γ -(Mn, Cu) and martensitic transformation of γ -(Mn, Cu) \rightarrow γ' -(Mn, Cu) can occur at $T_A = 400\text{--}480^\circ\text{C}$ in the SLM_{ED} Mn–30%Cu and at $T_A = 430^\circ\text{C}$ in the SLM_{ED} Mn–40%Cu.

Then, the lattice parameters of the face centered tetragonal (*f.c.t.*)- γ' phase (*a* and *c*) and *f.c.c.*- γ phase (*a*₀) were calculated as shown in Table 3 based on the XRD results in Figure 3. The SLM_{ED} Mn–xCu alloys have an *f.c.c.*- γ structure with lattice parameters in the range of *a*₀ = 3.710–3.777 Å. The tetragonal distortion value ($1 - c/a$) was obviously larger (>0.0200) in the SLM_{ED}+SA_{ED} Mn–30% Cu at $T_A = 400\text{--}430^\circ\text{C}$, as compared with other samples. The more significant tetragonal distortion always implies more martensitic transformation, more {101} twins, and a resulting higher damping capacity. Therefore, it means that $T_A = 400\text{--}430^\circ\text{C}$ is the more proper parameter of aging for the Mn–30% Cu, similar to the reported range (435°C) in the literature.^{13,18}

Controlling the microstructure by heat treatment

As discussed above, no martensitic transformation occurred in the as-SLM_{ED} Mn–xCu alloy. Therefore, heat treatment is indispensable to promote the formation of the γ' phase to improve the damping property. After aging treatment, the microstructure was mainly composed of the intragranular γ -(Mn, Cu) cellular dendrites and a small amount of α -Mn precipitates in Figure 4. With T_A increasing from 400°C to 530°C , DAS increased from ~ 0.9 to $\sim 4.2 \mu\text{m}$ and from ~ 0.9 to $\sim 2.8 \mu\text{m}$ in the Mn–40%Cu and Mn–30%Cu, respectively. When $T_A > 430^\circ\text{C}$, the spherical ($\sim 0.2 \mu\text{m}$ in diameter), cuboidal ($\sim 0.4 \mu\text{m}$ in size), and rod-like ($\sim 1.0 \mu\text{m}$ in length and $\sim 0.2 \mu\text{m}$ in diameter) α -Mn precipitates were as seen in Figure 4c, d, g, and h. The precipitation of α -Mn is usually the evidence of averaging. The microstructural optimization is limited only by aging treatment for the SLM_{ED} Mn–xCu alloy.

After SA treatment, the cellular dendrites of the alloys disappeared due to the occurrence of recrystallization process. The microstructures consisted of the equiaxed γ -(Mn, Cu) grains and some α -Mn precipitates within grains in the SLM_{ED}+SA_{ED} samples as in Figure 5. As shown in Table 4, the average grain size of equiaxed γ -(Mn, Cu) grains increased from ~ 89.4 to $\sim 113.4 \mu\text{m}$ and from ~ 72.4 to $\sim 103.3 \mu\text{m}$ in the SLM_{ED}+SA_{ED} Mn–40%Cu (Fig. 5a–d) and Mn–30%Cu samples (Fig. 5e–h) with increasing T_A from

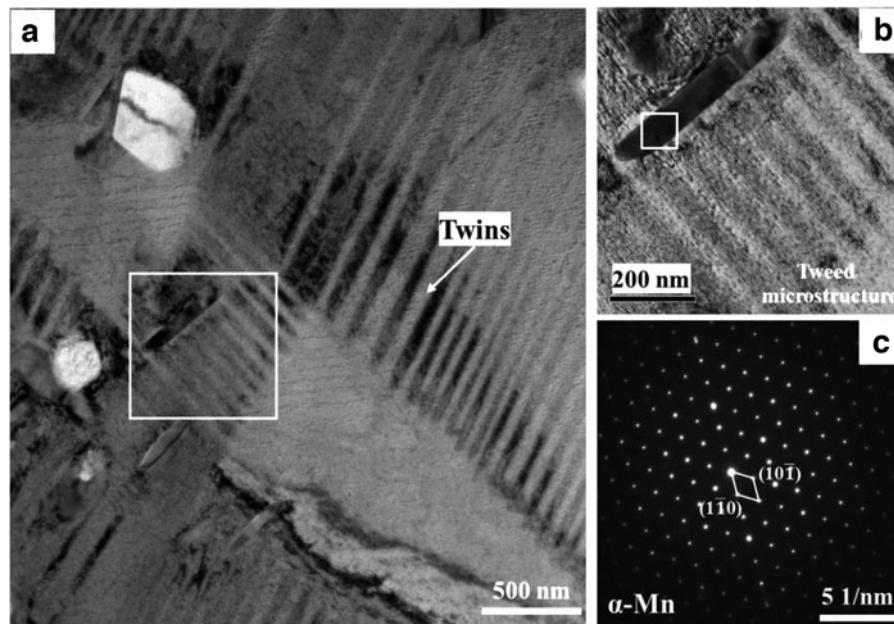


FIG. 6. TEM brightfield micrograph (a) of the SLM_{ED}+SA_{ED} Mn–30%Cu alloy at $T_A = 430^\circ\text{C}$; (b) is the magnification of the areas indicated by the yellow box indicated in (a); (c) is SAED pattern of the area indicated by the yellow box in (b). SAED, selected area electron diffraction; TEM, transmission electron microscope.

400°C to 530°C, respectively. Moreover, a large amount of rod-like α -Mn precipitates ($\sim 2.3 \mu\text{m}$ in length and $\sim 0.3 \mu\text{m}$ in diameter) were detected in the SLMed+SAed samples when $T_A > 430^\circ\text{C}$ (Fig. 5c, d, g, and h). A few nanoscale α -Mn phases can contribute to strength and hardness by precipitation strengthening. However, a large number of α -Mn precipitates certainly slow down the martensitic phase transformation and the formation of twins. Therefore, the aging temperature above 430°C may be detrimental to the SLMed Mn- x Cu samples.

Figure 6 is TEM micrographs of the SLMed+SAed Mn-30%Cu alloy at $T_A = 430^\circ\text{C}$. A high density of parallel twin plate structure and second-phase precipitates can be observed in Figure 6a. The formed twin plate structure may be the evidence of martensitic transformation in the sample. Moreover, the tweed microstructure within the twin striations

was also seen in Figure 6b, which is the typical characteristic of spinodal decomposition for Mn-Cu-based alloys. Based on the SAED pattern in Figure 6c, the rod-like precipitate was identified as the α -Mn phase. The existence of α -Mn precipitate may demonstrate that the enrichment degree of Mn in the Mn-rich zone may be nearly maximum in the sample.

APT has enabled to identify and spatially resolve the solute upon phase separation at the atomic scale. The 3D, 2D, and 1D APT reconstruction results of the SLMed+SAed Mn-30%Cu alloy at $T_A = 430^\circ\text{C}$ are shown in Figure 7. A second-phase precipitate can be found in zone I in 3D APT tip reconstruction in Figure 7a. Based on the 2D projections (Fig. 7b) and 1D composition profiles (Fig. 7c, d) of the Mn and Cu contents in the zone I, the precipitate containing nearly only the Mn element can be identified as α -Mn phase,

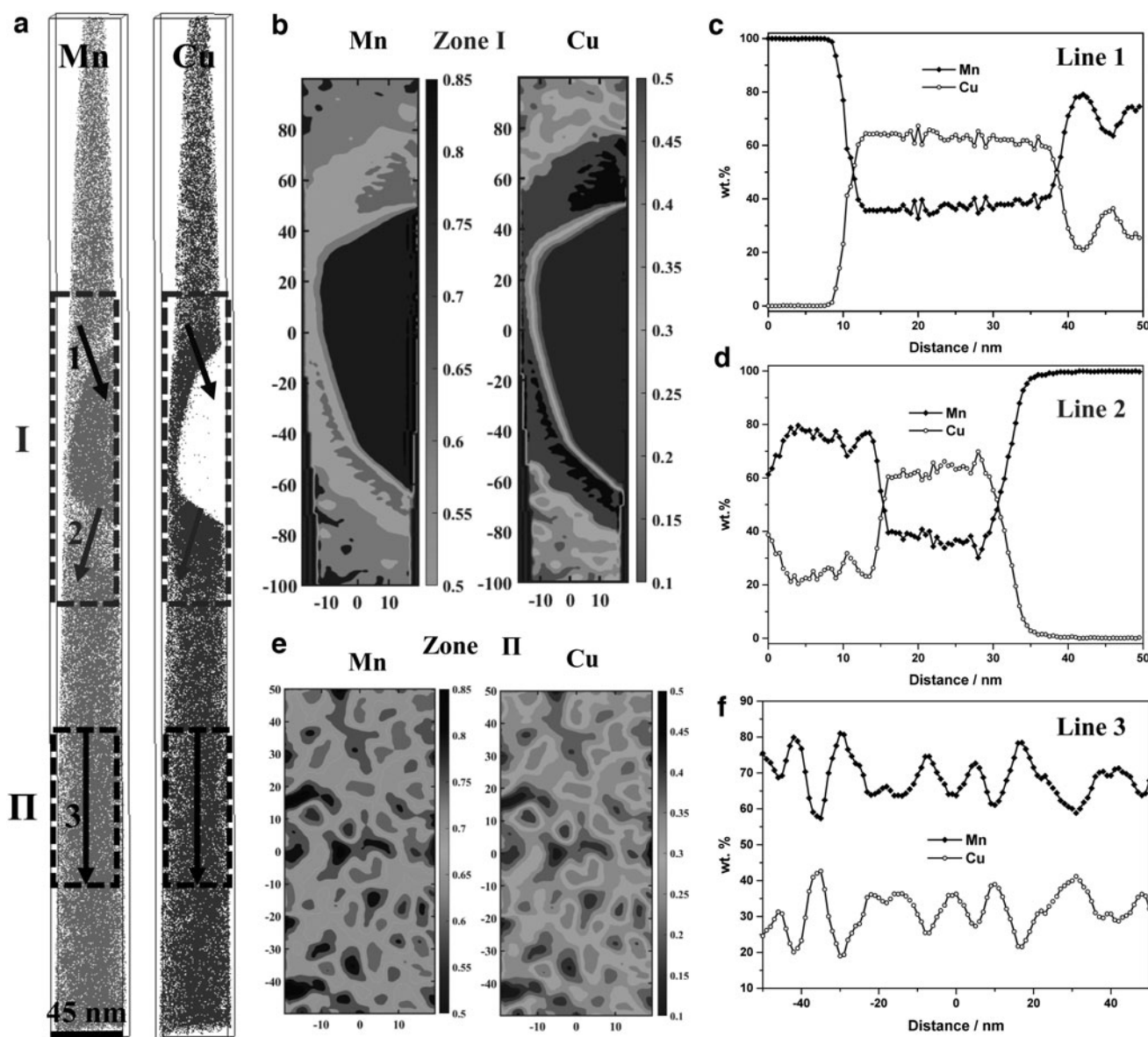


FIG. 7. (a) 3D APT tip reconstructions ($45 \times 45 \times 650 \text{ nm}^3$) of Mn and Cu in the SLMed+SAed Mn-30%Cu alloy at $T_A = 430^\circ\text{C}$; (b) and (e) are the 2D projections of the Mn and Cu concentration in the zones I and II marked in (a), respectively; (c, d, f) are the 1D composition profiles of the cylinder (10 nm in diameter) along the three arrows indicated in (a), respectively. APT, atom probe tomography.

TABLE 5. THE MICROSTRUCTURAL COMPARISONS BETWEEN THE SLMed AND TRADITIONAL THERMOMECHANICAL-PROCESSED MN-CU ALLOYS

Composition	Process	HT parameters	Phase
Mn-19.2Cu-4.9Ni-3.2Fe wt.% ³⁸ 70Mn24.95Cu3Al2Zn0.05Ce (at%) ³⁹ M2052 ⁴⁰	As-cast/As-VIM	—	Equiaxed γ dendrites (DAS = 4–44 μm)
Mn-20.53Cu-4.61Ni-1.9Fe at. % ⁴¹	As-quenched	900°C × 2 h-oil quenching 830°C × 1 h-salt quenching	Equiaxed γ (~31.3 μm)
Mn-19Cu-2Al-4Ni (wt.%) ⁸ Mn-26.0Cu-2.0Ni-2.0Fe- 2.0Zn-3.0Al ¹³	Aged Cast/VIM	435°C × 2–4 h	Equiaxed γ dendrites+ γ'
Mn-20.53Cu-4.61Ni-1.9Fe at. % ⁴¹ M2052 ⁴² 70Mn-24Cu-3Zn-3Al (at.%) ¹⁹ Mn-19Cu-2Al-4Ni (wt.%) ⁷	Casted/ VIMed+SAed	900°C × 2 h + 435°C × 6 h 850°C × 24 h + 430°C × 2 h 830°C × 1 h + (400–480°C) × (3–120 h) 850°C × 40 min + (400–520°C) × 8 h/440°C × (1–120 h)	Equiaxed γ (76–156.7 μm) + γ' + α
Mn-13Cu (wt.%) ¹⁷	As-SLMed	—	Cellular γ dendrite (DAS = 0.9–1.2 μm)
Mn-xCu (x = 30–40 wt.%)	Aged SLMed	(400–530°C) × (1–10 h)	Cellular γ dendrite (DAS = 0.9–4.2 μm)+ γ' + α
	SLMed+SAed	900°C × 1 h + (400–530°C) × 2 h	Equiaxed γ (72–113 μm) + γ' + α

DAS, dendritic arm spacing; HT, heat treatment; VIM, vacuum induction melting.

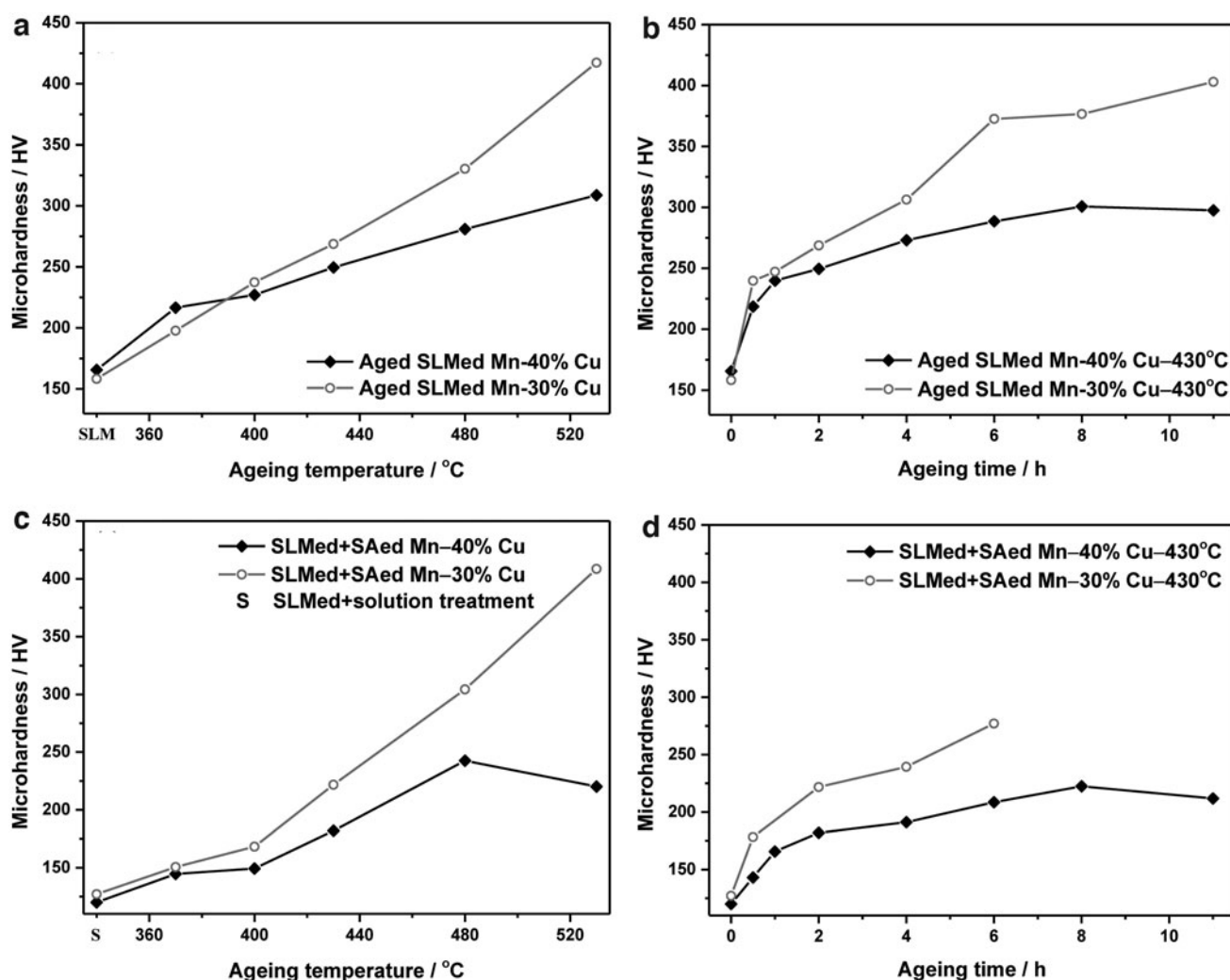


FIG. 8. The microhardness of the as-SLMed, aged SLMed (a, b), and SLMed+SAed (c, d) Mn-xCu alloys under various ageing temperatures (a, c) and time (b, d).

which was consistent with the results of TEM in Figure 6. Besides, the α -Mn precipitate was attached by a film of Cu-rich nanodomain with the thickness of 15–30 nm. Therefore, the α -Mn phase precipitated by fully squeezing out Cu atoms from the γ -(Mn, Cu) phase to form the considerable clustering of Mn atoms and a film of Cu-rich nanodomain attached to the precipitate in the Mn- x Cu alloys. The results are also consistent with our previous work.³⁷

The highly interconnected spinodal decomposition patterns were observed in the 2D projections of Mn and Cu contents in zone II (Fig. 7e). The nanoscale Mn-enrichment and Cu-enrichment regions can be clearly distinguished in terms of composition modulation. The wavelength of the compositional modulation was about 11.5 nm based on the 1D compositional profile (Fig. 7f), which was consistent with 10–20 nm in the previous work.^{2,38} Furthermore, it can be quantified that the fluctuation of Mn and Cu contents developed from ~ 81 wt% to 61 wt% and from 37 wt% to 22 wt%, respectively, in amplitude in the Mn-30%Cu alloy (Fig. 7f). So, the direct evidence for spinodal decomposition and second-phase precipitation of the Mn-Cu-based alloys was provided for the first time in the work.

Table 5 summarizes the microstructural comparisons between the SLMed and conventional thermomechanical-processed Mn-Cu alloys. The microstructures of both the as-SLMed and as-cast Mn-Cu-based alloys were mainly

composed of γ dendrite, but the DAS of the as-SLMed samples is one to two orders of magnitude smaller than those of the as-cast samples due to its more rapid cooling rate of SLM process. Moreover, the effects of heat treatment on the microstructural evolution are similar between the SLMed and casted/VIMed Mn-Cu alloys. But, the grain size (72–113 μm) of the SLMed+SAed samples is slightly smaller compared with casted/VIMed+SAed counterparts (76–156.7 μm). Compared with the casted Mn-Cu alloys, the SLMed samples seem to need a shorter aging time, probably because of their finer DAS.

Metastable miscibility gap and spinodal decomposition

The microhardness of the as-SLMed, aged SLMed, and SLMed+SAed Mn- x Cu alloys was shown in Figure 8. The microhardness is similar (150–165 Vickers microhardness [HV]) in the Mn- x Cu samples under the as-SLMed state. The microhardness was increased to be 216–309 and 198–417 HV with aging temperature in the aged SLMed Mn-40%Cu and Mn-30%Cu samples, respectively (Fig. 8a). The microhardness is ~ 120 HV in the SLMed Mn- x Cu samples under solution treatment conditions. The microhardness was first increased to 145–242 HV at $T_A = 370$ – 480°C and then decreased to 220 HV at $T_A = 530^\circ\text{C}$ in the SLMed+SAed Mn-40%Cu (Fig. 8c). In contrast, the microhardness was increased to 150–408 HV

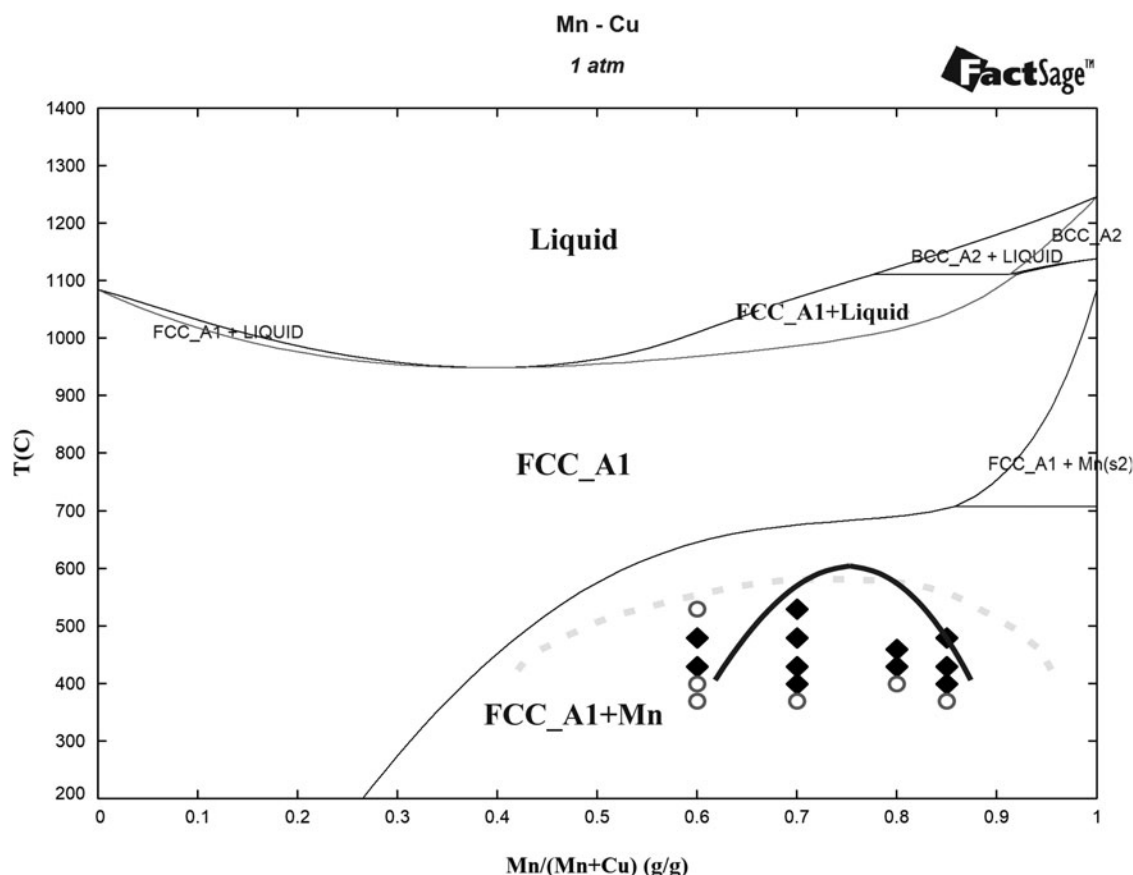


FIG. 9. Phase diagram of Mn-Cu system calculated by Factsage™; the solid and dashed lines are the metastable miscibility gaps calculated by thermodynamics in the present work and measured by hardness results from Vitek and Warlimont,⁴³ respectively; \blacklozenge and \circ represent compositions and temperatures within and outside miscibility gap from the microhardness results in the present work, respectively. BCC, body centered cube; FCC, face center cubic.

with aging temperature in the SLMed+SAed Mn-30%Cu alloy (Fig. 8c). The increase in microhardness in the aged SLMed and SLMed+SAed samples is due mainly to the precipitation hardening of the α -Mn phase and phase separation from spinodal decomposition.

According to the XRD results in Figure 3, α -Mn was not detected until aging 2 h at 480°C for SLMed+SAed Mn-30%Cu or 530°C for Mn-40%Cu alloys, respectively. Therefore, the apparent increases in microhardness for SLMed+SAed Mn-30%Cu at $T_A = 400$ –430°C and SLMed+SAed Mn-40%Cu at $T_A = 430$ –480°C in Figure 8c had taken place before α -Mn precipitation and corresponded to the phase separation of spinodal decomposition.

The microhardness was also increased to be 218–300 and 240–403 HV with increasing t_A from 0.5 to 11 h in the aged SLMed Mn-40%Cu and Mn-30%Cu at $T_A = 430$ °C, respectively (Fig. 8b). Moreover, the microhardness was increased to be 143–222 and 178–277 HV with t_A in the SLMed+SAed Mn-40%Cu and Mn-30%Cu at $T_A = 430$ °C, respectively (Fig. 8d). The microhardness is always higher in the Mn-30%Cu samples than those in the Mn-40%Cu samples under the same heat treatment states, resulting from the

higher contents of α -Mn precipitates in the Mn-30%Cu samples. Compared with SA treatment, the aging treatment can more obviously improve the microhardness due mainly to the higher contents of nanoscale α -Mn precipitates in the samples.

Aging at metastable miscibility gap can induce spinodal decomposition and martensitic transformation in the SLMed Mn-xCu alloys. Thus, the miscibility gap is essential to determine the heat treatment parameters. Figure 9 is the calculated phase diagram of the Mn-Cu system by FactsageTM. The metastable miscibility gap was studied by thermochemical modeling and hardness measurement in the work. The blue solid and green dashed lines in Figure 9 were the metastable miscibility gaps calculated by thermodynamics in the present work and measured by hardness results from Vitek and Warlimont,⁴³ respectively. The miscibility gap from hardness measurement is wider than that from thermodynamics calculation.

Aging an alloy within a miscibility gap to develop a two-phase structure by spinodal decomposition would be expected to give rise to an increase in hardness. Therefore, the criterion can be concluded to determine whether or not the compositions and temperatures lie within the miscibility

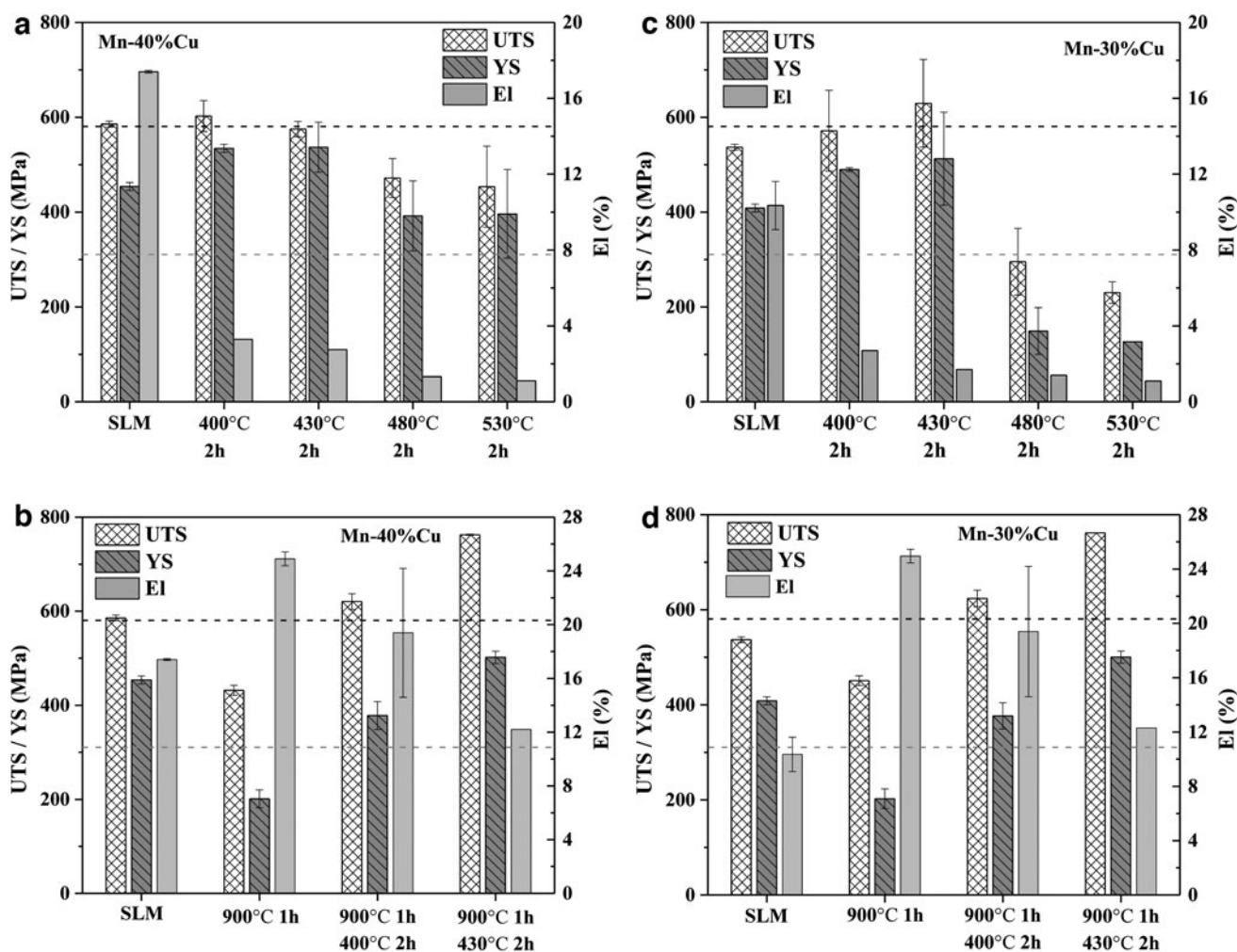


FIG. 10. The tensile properties of the as-SLMed, aged SLMed (a, c), and SLMed+SAed (b, d) Mn-40%Cu (a, b) and Mn-30%Cu (c, d) samples; the black and green dotted lines show the tensile and yield strength requirements of the as-cast Mn-Cu alloys, respectively. El, elongation; UTS, ultimate tensile strength; YS, yield strength.

gap. If the increase in microhardness of the Mn–Cu alloy during aging is before α -Mn precipitation, the aging temperatures for the compositions in question are within the miscibility gap. Applying the criterion to the present microhardness results in Figure 9; the miscibility gap from thermodynamics calculation seems to be basically consistent with the microhardness results for the SLMed Mn–Cu alloys.

Optimizing the tensile properties by heat treatment

Figure 10 is the ultimate tensile strength (UTS), yield strength (YS), and elongation (EI) extracted from the displacement–stress curves of the SLMed Mn–xCu alloys. The UTS and YS values of the as-SLMed Mn–40%Cu alloy reached the strength requirements, but its EI value (17.4%) is below the EI requirement (20%) of the as-cast Mn–Cu alloy. The UTS and EI values of the as-SLMed Mn–30%Cu alloy were lower than those of the as-cast Mn–Cu alloy. Compared with the as-SLMed samples, the strength values were first increased at $T_A = 400$ – 430°C and then decreased at $T_A = 480$ –

530°C (Fig. 10a and c) in the aged SLMed Mn–xCu alloys. Hence, 400 – 430°C was the proper aging temperature for the SLMed Mn–xCu alloys. Nevertheless, the EI values were significantly decreased ($<4\%$) in the aged SLMed Mn–xCu alloys. Hence, the tensile properties of the SLMed Mn–xCu alloys cannot be improved only by the aging treatment, which is consistent with the results in Controlling the Microstructure by Heat Treatment section.

After solution treatment at 900°C (Fig. 10b, d), the EI values ($\sim 25\%$) of the SLMed Mn–xCu alloys were increased to be above the EI requirement (20%) due to the formed equiaxed γ -(Mn, Cu) grains under recrystallization process. But their strength values were decreased to be well below the strength requirements. As compared with the aging treatment, the tensile properties of the Mn–xCu samples were enhanced by the SA treatment. The strength values of the SLMed+SAed Mn–xCu alloys were improved to be above the strength requirements at the expense of EI. The EI of the SLMed+SAed Mn–xCu alloys was still lower than the as-cast Mn–Cu alloy requirements. In addition, the fracture surface

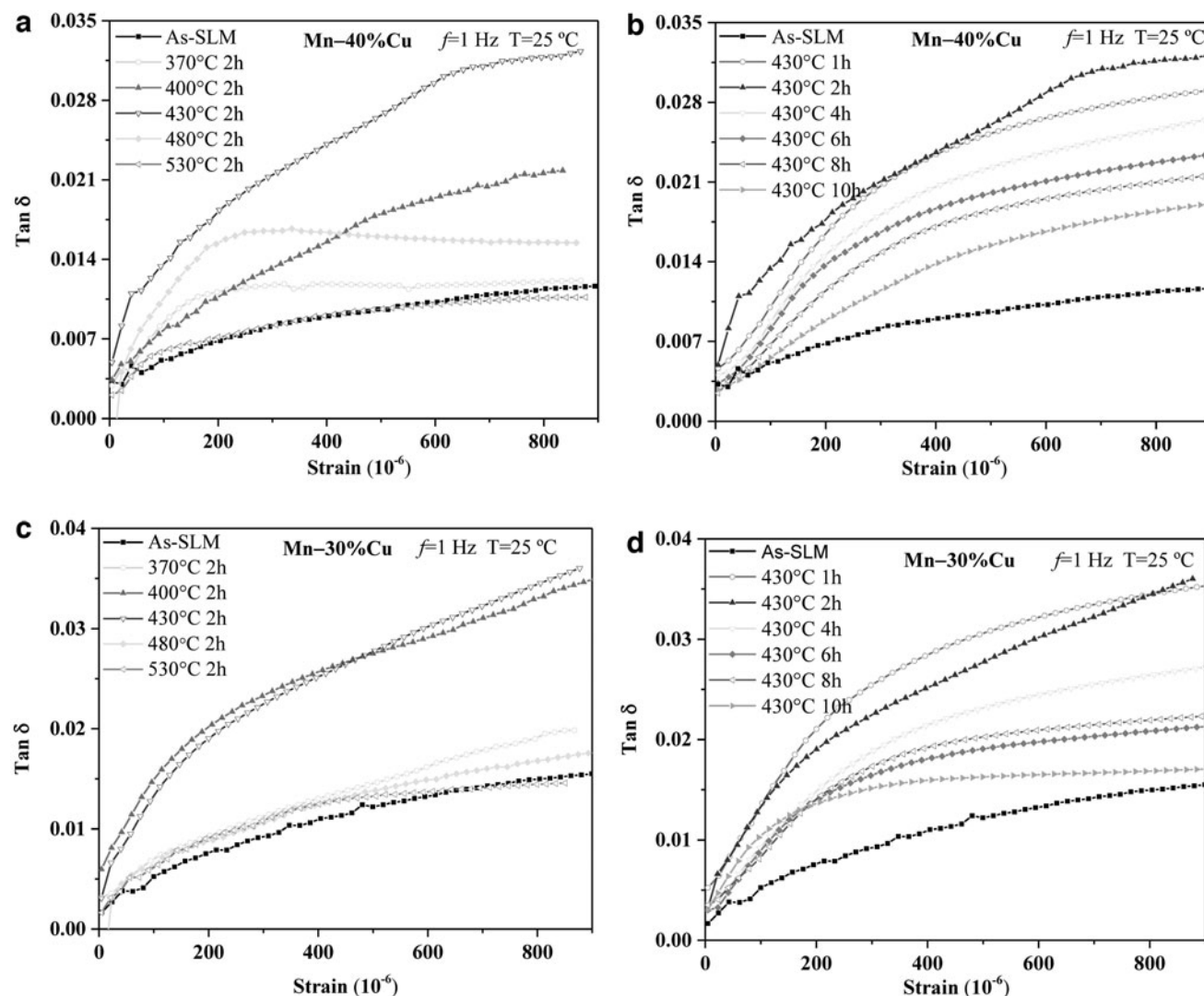


FIG. 11. The damping capacity values of the aged SLMed Mn–40%Cu (a, b) and Mn–30%Cu (c, d) alloys under various aging temperatures (a, c) and time (b, d).

morphologies of the as-SLMed, aged SLMed, and SLMed+SAed samples consisted of ductile dimple, which was a typical characteristic of ductile fracture.

Optimizing the damping properties by heat treatment

Figure 11 exhibited the damping capacity values ($\tan \delta$) of the as-SLMed and aged SLMed Mn-xCu alloys with a strain amplitude of $0-900 \times 10^{-6}$ at room temperature. The as-SLMed Mn-30%Cu samples ($\tan \delta=0-0.0158$ at strain amplitude of $0-900 \times 10^{-6}$) possessed a slightly higher damping capacity than those of the as-SLMed Mn-40%Cu sample ($\tan \delta=0-0.0116$). The damping capacity of the SLMed Mn-xCu alloys was improved by aging treatment at nearly the whole strain amplitude range. As compared with the as-SLMed counterpart, a ~ 2.8 times increase ($\tan \delta=0-0.0323$) in damping capacity occurred in the aged SLMed Mn-40%Cu samples at $T_A=430^\circ\text{C}$ in Figure 11a. The highest damping capacity values can be obtained in the aged SLMed Mn-40%Cu samples by the aging of $430^\circ\text{C} \times 2$ h. The aged SLMed Mn-30%Cu samples possessed a higher

damping capacity ($\tan \delta=0-0.0360$) at $T_A=400-430^\circ\text{C}$ compared with other aging temperatures (Fig. 11c).

The damping capacity decreased with increasing t_A from 2 to 10 h in the aged SLMed Mn-xCu samples (Fig. 11b, d). Compared with the as-SLMed counterpart, a ~ 2.3 times increase in the damping capacity was observed in the aged SLMed Mn-30%Cu samples by the aging of $400-430^\circ\text{C} \times 1-2$ h.

Figure 12 was the damping capacity of the SLMed+SAed Mn-xCu alloys. As compared with aging treatment, SA treatment can improve the damping capacity more obviously. The highest damping capacity values ($\tan \delta=0-0.0498$) can be obtained in the SLMed+SAed Mn-40%Cu samples by the aging at $430^\circ\text{C} \times 2$ h (Fig. 12a, b), which were ~ 4.3 times of those of the as-SLMed sample. Expectedly, the highest damping capacity values ($\tan \delta=0-0.0709$) of the SLMed+SAed Mn-30%Cu samples by the aging at $430^\circ\text{C} \times 1$ h (Fig. 12c, d), were ~ 4.5 times of those of the as-SLMed sample. The excellent damping capacity of the SLMed Mn-xCu alloys originated from the nanoscale Mn-enrichment regions formed during spinodal decomposition, which was consistent with the results of the microstructural evolution

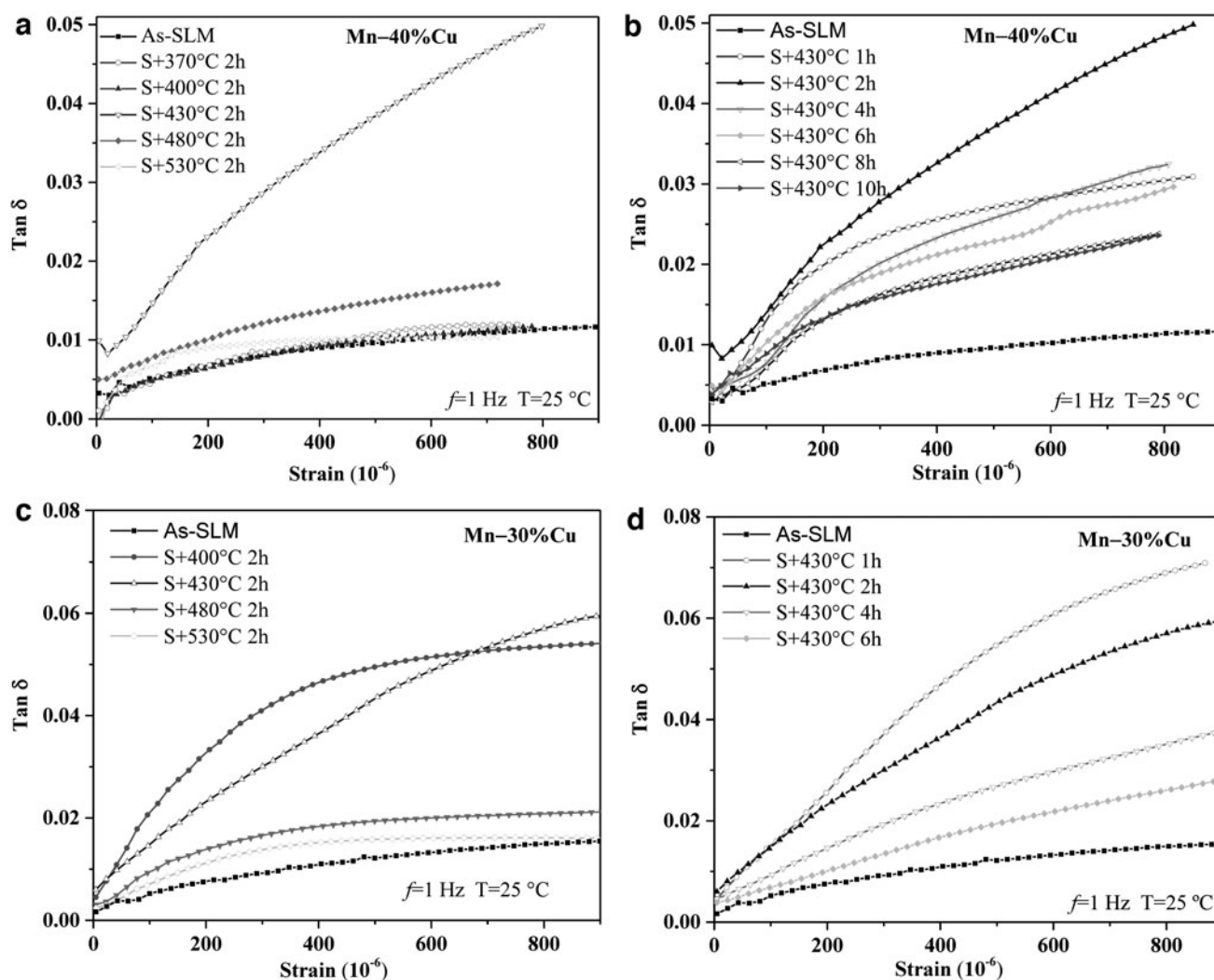


FIG. 12. The damping capacity values of the SLMed+SAed Mn-40%Cu (a, b) and Mn-30%Cu (c, d) alloys under various aging temperatures (a, c) and time (b, d); S represents solution treatment.

above. Hence, the proper aging temperature was 400–430°C for the SLMed Mn–30%Cu and 430°C for the SLMed Mn–40%Cu alloys, similar to the as-cast Mn–Cu alloys (435°C¹⁹). SA treatment of 900°C × 1 h + 430°C × 1–2 h is the relatively optimized heat treatment parameter for the SLMed Mn–xCu alloy.

Conclusions

In this work, SLM was first applied to directly realize the *in situ* synthesis of Mn–xCu ($x = 30\text{--}40$ wt.%) alloys based on the blended elemental powders. The effects of heat treatment on the microstructural evolution and damping property of the SLMed Mn–xCu samples were investigated. The main conclusions are as follows.

- (1) Mn–xCu alloys show good processability of laser additive manufacturing based on the blended elemental powders. The γ -(Mn, Cu) phase with DAS of 0.9–1.2 μm was the main constituent phase in the as-SLMed samples, which was one to two orders of magnitude finer than those of the as-cast samples.
- (2) Aging at 400–480°C for the Mn–30%Cu or 430°C for Mn–40%Cu alloys can induce spinodal decomposition, martensitic transformation, and α -phase precipitation, whose direct evidence was provided for the first time by transmission electron microscopy and 3D APT in the work. Compared with the casted alloys, the SLMed Mn–xCu samples need a shorter aging time (1–2 h).
- (3) The microhardness was increased with aging temperature and time in the aged SLMed and SLMed+SAed samples due mainly to the contribution from the α -Mn precipitation and spinodal decomposition. The miscibility gap obtained from thermodynamics calculation was basically consistent with the microhardness results for the SLMed Mn–xCu alloys.
- (4) The 2.3–2.8 times and 4.3–4.5 times increase in damping capacity were obtained in the aged SLMed and SLMed+SAed Mn–xCu samples, respectively. SA treatment of 900°C × 1 h + 430°C × 1–2 h was the relatively optimized heat treatment parameter for the SLMed Mn–xCu alloy, resulting in a higher damping capacity ($\tan \delta = 0.0709$ and 0.0498 at a strain amplitude of 900×10^{-6} for Mn–30%Cu and Mn–40%Cu, respectively) and tensile properties (764 MPa, 540 MPa, and 12.5% for Mn–30%Cu, and 762 MPa, 501 MPa, and 12.9% for Mn–40%Cu).

Author Disclosure Statement

No competing financial interests exist.

Funding Information

This work was supported by the National Natural Science Foundation of China Program (no. 51805186), Fundamental Research Funds for the Central Universities (no. 20420 21kf0033), the Open Project Program of Wuhan National Laboratory for Optoelectronics NO. 2021WNLOKF0009, and Postdoctoral Research Foundation of China Program-funded projects (nos. 2017M620317 and 2018T110759).

References

1. Nosova G, Vintaikin E. Investigation of nature of two-way shape memory effect in γ -Mn based alloys. *Scripta Mater* 1999;40:347–351.
2. Yin F, Ohsawa Y, Sato A, *et al.* Phase decomposition of the γ phase in a Mn–30 at.% Cu alloy during aging. *Acta Mater* 2000;48:1273–1282.
3. Li D, Liu W, Li N, *et al.* Remarkable improvement of damping capacity of Mn–20Cu–5Ni–2Fe (at%) alloy by zinc element addition. *Adv Eng Mater* 2017;19:1700437.
4. Wei L, Li Q, Zhang X, *et al.* Remarkable improvement in damping capacity of M2052 alloy by step-cooling treatment. *Mater Res Express* 2021;8:016526.
5. Zuo S, Xiao F, Fukuda T. Orientation dependence of damping behavior in a Mn–Cu shape memory alloy. *Scripta Mater* 2019;170:95–98.
6. Shi S, Liu C, Wan J, *et al.* Thermodynamics of fcc–fct martensitic transformation in Mn–X (X = Cu, Fe) alloys. *Mater Des* 2016;92:960–970.
7. Sun L, Vasin R, Islamov AK, *et al.* Influence of spinodal decomposition on structure and thermoelastic martensitic transition in MnCuAlNi alloy. *Mater Lett* 2020;275:128069.
8. Yan J, Li N, Fu X, *et al.* The strengthening effect of spinodal decomposition and twinning structure in MnCu-based alloy. *Mater Sci Eng A* 2014;618:205–209.
9. Oliveira JP, Crispim B, Zeng Z, *et al.* Microstructure and mechanical properties of gas tungsten arc welded Cu–Al–Mn shape memory alloy rods. *J Mater Process Tech* 2019;271:93–100.
10. Lu F, Wu B, Zhang J, *et al.* Microstructure and damping properties of MnCuNiFeCe alloy. *Rare Met* 2016;35:615–619.
11. Yin F, Ohsawa Y, Sato A, *et al.* X-ray diffraction characterization of the decomposition behavior of γ Mn phase in a Mn–30at.% Cu alloy. *Scripta Mater* 1999;40:993–998.
12. Zhao C, Yang J, Li G, *et al.* Laser powder bed fusion of the Mn–Cu alloys: Printability, microstructure, and mechanical properties. *J. Alloys Compd* 2022;899:163385.
13. Liu W, Li N, Zhong Z, *et al.* Novel cast-aged MnCuNi–FeZnAl alloy with good damping capacity and high usage temperature toward engineering application. *Mater Des* 2016;106:45–50.
14. Chevalier Y. Damping in materials and structures: An overview. In: Altenbach H, Pouget J, Rousseau M, Collet B, Michelitsch, T, eds. *Generalized Models and Non-classical Approaches in Complex Materials*, vol. 2. Springer, Cham, Switzerland. 2018; pp. 1–27.
15. Deng C, Peng W, Xiong Z, *et al.* Spinodal decomposition and martensitic transformation kinetics of the 82.2 Mn–15.8 Cu–2Al thermosensitive damping alloy. *Thermochim Acta* 2020;683:178321.
16. Sakaguchi T, Yin F. Holding temperature dependent variation of damping capacity in a MnCuNiFe damping alloy. *Scripta Mater* 2006;54:241–246.
17. Sun L, Sumnikov S, Islamov AK, *et al.* Spinodal decomposition influence of austenite on martensitic transition in a Mn–13 at.% Cu alloy. *J Alloys Compd* 2021;853:157061.
18. Zhong Z, Liu W, Li N, *et al.* Mn segregation dependence of damping capacity of as-cast M2052 alloy. *Mater Sci Eng A* 2016;660:97–101.
19. Zhang S, Guo XP, Tang Y, *et al.* Microstructure and properties of Mn–Cu-based damping alloys prepared by ball

- milling and hot-press sintering. *J Mater Eng Perform* 2019;28:2641–2648.
20. Nosova GI. FCC → FCT martensitic transformation in two-phase Mn–Cu alloys. *Russian Metallurgy (Metally)* 2017;3:216–220.
 21. Wang C, Liu X, Ohnuma I, *et al.* Thermodynamic assessments of the Cu–Mn–X (X: Fe, Co) systems. *J Alloys Compd* 2007;438:129–141.
 22. Hou S, Qin F, Han J, *et al.* Strain glass transition in high damping Mn-22Cu-5Ni-2Fe alloy. *Prog Nat Sci Mater* 2018;28:614–617.
 23. Oliveira JP, LaLonde AD, Ma J. Processing parameters in laser powder bed fusion metal additive manufacturing. *Mater Des* 2020;193:108762.
 24. Antunes LHM, Hoyos JJ, Andrade TC, *et al.* Deformation-induced martensitic transformation in Co-28Cr-6Mo alloy produced by laser powder bed fusion: Comparison surface vs. bulk. *Addit Manuf* 2021;46:102100.
 25. Conde FF, Avila JA, Oliveira JP, *et al.* Effect of the as-built microstructure on the martensite to austenite transformation in a 18Ni maraging steel after laser-based powder bed fusion. *Addit Manuf* 2021;46:102122.
 26. Zhang J, Gao J, Bo S, *et al.* A novel crack-free Ti-modified Al-Cu-Mg alloy designed for selective laser melting. *Addit Manuf* 2021;38:101829.
 27. Yang J, Yu H, Yang H, *et al.* Prediction of microstructure in selective laser melted Ti6Al4V alloy by cellular automaton. *J Alloys Compd* 2018;748:281–290.
 28. Su C, Yu H, Wang Z, *et al.* Controlling the tensile and fatigue properties of selective laser melted Ti–6Al–4V alloy by post treatment. *J Alloys Compd* 2021;857:157552.
 29. Zhang S, Guo X, Tang Y, *et al.* A comparative study on microstructure and damping capacity of Mn–Cu based alloys with dendrite and equiaxial grain. *Vacuum* 2019;168:108814.
 30. Yang H, Yang J, Huang W, *et al.* Controllable in-situ aging during selective laser melting: Stepwise precipitation of multiple strengthening phases in Inconel 718 alloy. *J Mater Sci Technol* 2019;35:1925–1930.
 31. Yang J, Li F, Pan A, *et al.* Microstructure and grain growth direction of SRR99 single-crystal superalloy by selective laser melting. *J Alloys Compd* 2019;808:151740.
 32. Fan J, Zhang L, Wei S, *et al.* A review of additive manufacturing of metamaterials and developing trends. *Mater Today* 2021;50:303–328.
 33. Yang J, Han J, Yu H, *et al.* Role of molten pool mode on formability, microstructure and mechanical properties of selective laser melted Ti-6Al-4V alloy. *Mater Des* 2016;110:558–570.
 34. Luo S, Huang W, Yang H, *et al.* Microstructural evolution and corrosion behaviors of Inconel 718 alloy produced by selective laser melting following different heat treatments. *Addit Manuf* 2019;30:100875.
 35. Dinsdale AT. SGTE data for pure elements. *Calphad* 1991;15:317–425.
 36. Turchanin MA, Agraval PG, Abdulov AR. Phase equilibria and thermodynamics of binary copper systems with 3 d-metals. IV. Copper-manganese system, *Powder Metall Met C* 2006;45:569–581.
 37. Yang J, Zhao C, Liang H, *et al.* Spinodal decomposition and martensitic transformation of the high manganese Mn–*x*Cu alloys fabricated by additive manufacturing. *Appl Mater Today* 2021;25:101170.
 38. Jiang Z, Hou L, Tian Q, *et al.* Polymorphic microstructure of a MnCu damping alloy solidified under magnetic field. *Mater Res Express* 2019;6:0865h2.
 39. Zhang S, Guo X, Zhong S, *et al.* The role of dendritic morphology and segregation in fcc-fct transformation and damping capacity of Mn–Cu based alloys. *Mater Trans* 2019;60:2298–2304.
 40. Yin F, Iwasaki S, Sakaguchi T, *et al.* Susceptibility of damping behavior to the solidification condition in the as-cast M2052 high-damping alloy. *Key Eng Mater* 2006;319:67–72.
 41. Jiang Z, Zhang S, Tian Q, *et al.* Phenomenological representation of mechanical spectroscopy of high damping MnCuNiFe alloy. *Mater Sci Technol* 2020;36:743–749.
 42. Jiang Z, Tian Q, Ren Z, *et al.* Development and characterization of a MnCu-based high damping alloy plate. *Mater Sci Technol* 2019;542:012020.
 43. Vitek J, Warlimont H. On a metastable miscibility gap in γ -Mn–Cu alloys and the origin of their high damping capacity. *Metal Sci* 1976;10:7–13.

Address correspondence to:
Jingjing Yang

The Institute of Technological Sciences
Wuhan University
Wuhan 430071
China

E-mail: jjyang0803@whu.edu.cn